

The M Dwarf GJ 436 and its Neptune-Mass Planet

H. L. Maness¹, G. W. Marcy¹, E. B. Ford¹, P. H. Hauschildt², A. T. Shreve³, G. B. Basri¹,
R. P. Butler⁴, S. S. Vogt⁵

Received _____; accepted _____

Accepted to PASP: 07 Nov 2006

arXiv:astro-ph/0608260v2 4 Dec 2006

¹Department of Astronomy, University of California at Berkeley, Berkeley, CA, USA 94720

²Hamburger Sternwarte, Gojenbergsweg 112, 21029 Hamburg, Germany

³College of Chemistry, University of California at Berkeley, Berkeley, CA, USA 94720

⁴Department of Terrestrial Magnetism, Carnegie Institution of Washington, 5241 Broad Branch Rd NW, Washington DC, USA 20015-1305

⁵UCO/Lick Observatory, University of California at Santa Cruz, Santa Cruz, CA, USA 95064

ABSTRACT

We determine stellar parameters for the M dwarf GJ 436 that hosts a Neptune-mass planet. We employ primarily spectral modeling at low and high resolution, examining the agreement between model and observed optical spectra of five comparison stars of type, M0-M3. Modeling high resolution optical spectra suffers from uncertainties in TiO transitions, affecting the predicted strengths of both atomic and molecular lines in M dwarfs. The determination of T_{eff} , gravity, and metallicity from optical spectra remains at $\sim 10\%$. As molecules provide opacity both in lines and as an effective continuum, determining molecular transition parameters remains a challenge facing models such as the PHOENIX series, best verified with high resolution and spectrophotometric spectra. Our analysis of GJ 436 yields an effective temperature of $T_{\text{eff}} = 3350 \pm 300$ K and a mass of $0.44 M_{\odot}$. New Doppler measurements for GJ 436 with a precision of 3 m s^{-1} taken during 6 years improve the Keplerian model of the planet, giving a minimum mass, $M \sin i = 0.0713 M_{\text{JUP}} = 22.6 M_{\text{Earth}}$, period, $P = 2.6439$ d, and $e = 0.16 \pm 0.02$. The noncircular orbit contrasts with the tidally circularized orbits of all close-in exoplanets, implying either ongoing pumping of eccentricity by a more distant companion, or a higher Q value for this low-mass planet. The velocities indeed reveal a long term trend, indicating a possible distant companion.

Subject headings: stars: individual (GJ 436, HIP 57087, LHS 310) – stars: fundamental parameters – stars: low mass – planetary systems

1. Introduction

To date, radial velocity surveys have revealed three exoplanetary systems with M dwarf hosts: GJ 876, GJ 436, and GJ 581 (Rivera et al. 2005; Butler et al. 2004; Bonfils et al. 2005b). Remarkably, all three of these M dwarfs host planets with minimum masses ($M \sin i$) less than $0.1 M_{\text{JUP}}$, ranking them among the lowest mass exoplanets known. Microlensing surveys have strengthened the case for the preferential occurrence of such “super-Earths” around M dwarfs. Current results suggest four M dwarf systems, with two harboring planets in the super-Earth mass range (Beaulieu et al. 2006; Gould et al. 2006; Bond et al. 2004; Udalski et al. 2005). Given detection biases against the discovery of low mass planets, all these findings imply that super-Earths are more common close companions to M dwarfs than gas giants (Endl et al. 2006; Beaulieu et al. 2006). The frequency of longer period planets remains poorly constrained.

From a theoretical viewpoint, the growth of planets around low mass stars has been explored only recently. Low mass stars likely form by accretion at the centers of protoplanetary disks having lower mass than those surrounding solar mass stars. Such low mass disks may spawn low mass planets, both because of less available mass and because of shorter survival times for the disks (Laughlin et al 2004). However, core accretion models of giant planet formation that include growth of a rocky core from dust particles followed by the gravitational accretion of gas suggest that giant planets may have enough time to form. Solutions to the time scale competition between planet growth and disk lifetime have been proposed by invoking both migration to move the planet to gas-rich areas and also by adopting lower opacities to allow faster accretion of the envelope onto the core (Hubickyj et al. 2004, Alibert et al. 2005). Nonetheless, rocky cores that are starved of gas may instead become ice giants similar to Neptune and Uranus (Goldreich et al. 2004, Thommes et al. 2002, Ida & Lin 2005). Under the core accretion paradigm, it remains unknown how commonly planets fail to accrete gas after successful growth of a rock and ice core, thereby leaving behind a super-Earth planet. Most recently, Boss (2006) provided a very different viable alternative to the core accretion scenario, showing that disk instability can also be invoked to explain current M dwarf observations. Distinguishing between these competing models of planet formation requires more observational results.

To further understanding in this area, we present a follow-up study of GJ 436, an M dwarf recently discovered to host a Neptune-mass planet ($M \sin i = 0.066 M_{\text{JUP}}$; Butler et al. 2004). At present, little is known about this system. As there is no other giant planet within a few AU of the host star, a larger planet cannot easily be invoked to explain a curtailed accretion of gas of the known planet, hereafter GJ 436b. Furthermore, since the stellar luminosity and mass are not well known, the planet’s minimum mass and predicted temperature are poorly constrained. To better characterize this system, we have obtained new Doppler measurements and attempted to deduce accurate stellar parameters. In §2, we discuss photometric observations leading to estimates of the stellar mass and luminosity. In §3, we present an effort to determine the effective temperature, surface gravity, and metallicity of GJ 436 via low and high resolution spectral modeling. In §4, new Doppler

measurements are presented, leading to an improved orbit and minimum mass for the planet. In §5 and 6, we discuss the implications of our results.

2. Photometric Observations and Analysis

We first assess the stellar properties of GJ 436 using photometric measurements and published calibrations. We use optical and near-infrared photometry for GJ 436 taken from the compilation by Leggett (1992). The quoted values are $V = 10.66$, $I = 8.28$, $J = 6.93$, $H = 6.34$, and $K = 6.10$. We adopt the Hipparcos parallax for GJ 436 of 97.73 mas (Perryman et al. 1997).

2.1. Stellar Mass

We estimate the mass of GJ 436 from various empirical mass-luminosity relations (MLRs) and theoretical models for M dwarfs. Delfosse et al. (2000) have determined empirical MLRs for visual and near-infrared magnitudes using their newly discovered M dwarf binaries. With these relations, the V, J, H, and K band photometry from Leggett (1992) yield inferred masses for GJ 436 of 0.418, 0.439, 0.441, and 0.442 M_{\odot} , respectively. Thus, the JHK photometric calibrations all yield a stellar mass of $M_{\star} = 0.44 \pm 0.04 M_{\odot}$. We adopt an accuracy of $\sim 10\%$ in stellar mass from the scatter in the calibrations of Delfosse et al. (2000). The V band estimate of 0.418 M_{\odot} is lower than the mass derived from the the JHK calibration, but the V-band calibration has more scatter. Moreover, the particular metallicity of GJ 436 will affect the mass estimate from the V band more than from the IR bands. As metallicity remains somewhat uncertain (§3), we give more weight to the mass from the near-IR calibrations.

For comparison, the mass estimates derived from both the empirical relations of Henry & McCarthy (1993) and Benedict et al. (2001) agree within 10% of 0.44 M_{\odot} . The theoretical models of Baraffe et al. (1998) and Siess et al. (2000) applied to GJ 436 also yield masses that are in agreement at the 10% level, though the theoretical relation between mass and optical flux has a strong metallicity dependence. Here, we adopt the mass derived from the near-infrared relations of Delfosse et al. (2000), giving $M_{\star} = 0.44 \pm 0.04 M_{\odot}$. This value is 7.3% higher than that adopted by Butler et al. (2004), who gave more weight to the mass derived from the various V band calibrations.

2.2. Stellar Luminosity

Extensive observational analyses of M dwarf luminosities have been performed by Leggett et al. (1996), who derived luminosities for 16 M dwarfs by combining spectrophotometry and broadband measurements over the wavelength range, 0.35 to 5

μm . Reid & Hawley (2000) have fit second-order polynomials to the derived bolometric corrections of Leggett et al. (1996) in the V, I, and K bands. Employing these relations for GJ 436 yields implied luminosities of 0.024, 0.024, and 0.025 L_{\odot} , respectively.

These estimates are in good agreement with those derived from the tight empirical relation between M_K and M_{BOL} of Veeder (1974). The observed relations for luminosity are also in agreement with those from theoretical models constructed by Baraffe et al. (1998), Siess et al. (2000), and D’Antona & Mazzitelli (1994). Here, we assume the simple average of the derived luminosities quoted above: $L = 0.024 \pm 0.004 L_{\odot}$, slightly lower than the value, $L=0.025 L_{\odot}$, that was found by Butler et al. (2004).

3. Spectral Modeling

3.1. Model Atmospheres

To constrain the effective temperature, metallicity, and surface gravity of GJ 436, we compared observed spectra obtained at both low and high resolution to synthetic spectra. We used an updated grid of the NEXTGEN set of M dwarf models (Hauschildt et al. 1999) that includes an updated molecular line list, a revised treatment of dust grain formation, and a treatment of spherical geometry. A detailed description of the model atmospheres used in calculating the synthetic spectra presented here can be found in Allard et al. (2001).

3.2. High Resolution Modeling

We obtained high resolution ($R \sim 60,000$) echelle spectra for GJ 436 and five comparison M dwarfs (GJ 411, GJ 424, GJ 752A, GJ 860 A, and GJ 908) using the Keck 1 telescope with the HIRES spectrometer between June 1997 and November 2001. The wavelength range was 3700-6200 Å, contained in 33 spectral orders. Only spectra at wavelengths greater than 5203 Å were used in spectral modeling. The standard planet-hunting procedure for reduction of the raw echelle images was employed to perform flat-fielding, sky subtraction, order extraction, and wavelength calibration (Butler et al. 1996; Vogt et al. 1994). All spectral modeling was performed on template spectra not containing iodine.

To compare the observations to the models, several adjustments were made to the continuum and wavelength scale of the observed spectra. The pseudo-continuum levels of the M dwarf spectra consist of overlapping molecular bands, and the echelle spectra are not flux calibrated. To bring the models and the observed spectra to the same continuum value, we fit a second degree polynomial to the points of highest flux across each echelle order and also to the corresponding wavelength section of the model spectrum. We then divided by these pseudo-continuum polynomials to obtain normalized fluxes for both observed and synthetic spectra. We next degraded the resolution of the model spectra to match the observed resolution by convolving each model spectrum with a Gaussian of the appropriate

width. It was not necessary to modify the models further to correct for rotational line broadening, as none of the stars in our sample have significant rotation, having $V \sin i < 3 \text{ km s}^{-1}$ (Delfosse et al. 1998). Finally, we removed the stellar Doppler shift from the observed spectra by cross-correlating the observed and model spectra and shifting the observed spectra by the appropriate amount.

Comparing observed to synthetic spectra constitutes a standard approach in determining M dwarf stellar parameters (Jones et al. 1994; Leggett et al. 1996; Valenti et al. 1998; Basri et al. 2000; Leggett et al. 2000, 2001, 2002; Kirkpatrick et al. 1993; Bean et al. 2006). However, deducing characteristics of early type M dwarfs using high resolution spectral modeling has been performed rarely and has revealed uncertainties with the molecular constants (Valenti et al. 1998). To derive characteristics of GJ 436 from high resolution spectral modeling, we therefore tested the integrity of our model fits by tests on other early type M dwarfs. The comparison M dwarfs were selected to encompass the range of early spectral types and metallicities near GJ 436.

The results of our high resolution modeling of GJ 436 are summarized in Figure 1, showing overplotted synthetic and observed spectra for a representative portion of one echelle order. Figure 1 demonstrates that the model TiO lines, constituting a pseudo-continuous opacity for M dwarfs in the optical, do not match the observed molecular lines. This discrepancy was observed in all orders and for all M dwarfs in our sample. The specific wavelengths and pattern of wavelengths of the observed TiO lines is so different from those in the synthetic spectrum that no association of the two sets of TiO lines was possible. The apparent flaws in the molecular constants for TiO are reminiscent of those described for TiO by Valenti et al. (1998) in their high resolution spectra of M dwarfs. Apparently, the treatment of TiO at high resolution remains inadequate. We, therefore, decided that only the atomic lines could be used in modeling the observed echelle spectra.

With this limitation, the observed echelle spectra were compared to the model spectra in two ways. First, we examined each spectral order by eye against the model spectra, concentrating on the depths and wings of atomic lines, identified using a solar atlas. We monitored, but gave little weight to, the average strengths of the molecular lines. We considered only the strong atomic lines with equivalent widths greater than 0.1 \AA , which suffer little contamination from any blended TiO lines. Second, we performed a least squares fit to the strong atomic lines (giving no weight to the TiO lines). We extracted a small segment of spectrum centered on each atomic line extending three line widths on both sides of line center. In some cases, the observed atomic lines were significantly blended with molecular lines. These lines were not included in the least squares fit. To avoid unphysical results due to degeneracy in the three free parameters (temperature, metallicity, and surface gravity), we fixed the metallicities of our sample stars to match the results of Bonfils et al. (2005a) listed in Table 1. These metallicities were in all cases consistent with our classifications by eye.

Table 2 lists the derived temperatures from the spectral modeling for the six M dwarfs examined here. The first and second columns give the star name and spectral type. The

fourth and fifth columns list our derived values of T_{eff} from the high resolution spectra found by eye and by least squares fitting, respectively. For all stars but one (GJ 424), the estimates by eye are within 60 K of the results derived by least squares fitting, suggesting that our two fitting procedures are self-consistent. For GJ 424, the two methods gave T_{eff} different by 150 K. We note that the temperatures derived were nearly the same among all echelle orders fitted for a given star, also suggesting self-consistency.

The top panel in Figure 1 shows the best fit to GJ 436 for the high resolution modeling ($T_{\text{eff}} = 3200$ K, $\log g = 4.0$, $[M/H] = 0.0$), obtained both by least squares fitting and by eye. The observed and synthetic atomic line depths are similar in this model, and the overall strength of the molecular lines match well. But note that the TiO lines that pervade the spectrum do not correspond in detail, as discussed above. The Lorentzian line wings of the Ca I line at 6122 Å are also well matched. However, while the best fit model spectrum appears to match the observed atomic lines and the strength of the molecular lines, the surface gravity derived is significantly lower than the known surface gravities of M dwarfs, $\log g \sim 4.75$. This underestimate of surface gravity was consistently observed in high resolution modeling of all the M dwarfs in our sample, if we let $\log g$ float. Columns 4 and 5 of Table 3 demonstrate this bias towards low surface gravities, showing that in all cases the best fit to surface gravity yielded $\log g \leq 4.5$.

To investigate this discrepancy in gravity further, we fixed the surface gravity in our high resolution modeling to higher, and more likely, values than those that appear to best fit the models. Both $\log g = 4.5$ and $\log g = 5.0$ were tested. The second and fourth panels in Figure 1 display representative results obtained from this test with surface gravity fixed to $\log g = 5.0$. The strengths of the atomic lines are well-matched in the second panel, notably those between 6135 and 6143 Å. However, the Lorentzian line wings of the Ca I line at 6122 Å are too pronounced. The overall strength of the TiO lines also appear too weak in this model, though this discrepancy is more pronounced in other echelle orders. Similar results were observed for all stars in our sample. Specifically, for realistic values of surface gravity, we were unable to find models that simultaneously matched the observed atomic line profiles and the overall strength of the TiO lines.

We believe this anomaly is due to inaccuracy in the continuous opacity of the models. For M dwarfs observed in the optical, the dominant source of continuous opacity is TiO. Problems due to treatment of TiO are immediately seen in the lack of agreement between the resolved lines in the observed and model spectra. The pattern of model and observed TiO lines do not agree, suggesting significant errors in the model of the TiO energy levels, as noted previously by Valenti et al. (1998). Moreover, TiO molecules, in their role as an effective continuous opacity source, affect the predicted atomic line depths. Increased continuous opacity causes the $\tau = 2/3$ surface of the star to reside higher in the star’s atmosphere where the temperature is lower. In the LTE interpretation, the source function is the Planck function, which is lower due to the lower temperature. The atomic lines form in a similarly cool region and are thus less deep relative to the continuum.

However, increasing the surface gravity is degenerate with increasing the continuous

opacity, as larger gravity results in a larger TiO abundance. This effect is seen in the model spectra. Increasing the assumed surface gravity reduces the model atomic line depths (e.g. see panels 1 and 2 or 3 and 4 of Figure 1). Therefore, if the amount of continuous opacity in the models is effectively too high, the surface gravity need not be as high in order for the atomic line depths to match. As a result, the best fit surface gravities will be too low. This effect may explain the modeling bias towards low surface gravities discussed above.

In addition, we note that if the derived surface gravities are in error, the derived effective temperatures will also be in error (Buzzoni et al. 2001). For medium-high resolution spectral modeling, Buzzoni et al. (2001) have quantified the coupling between errors in derived surface gravity and those in effective temperature:

$$\frac{\Delta \log g}{\Delta T_{\text{eff}}} = 1.3 \left(\frac{1000}{T_{\text{eff}}} \right)^4 \text{ dexK}^{-1}$$

According to this relation, a decrease in surface gravity of ~ 1.0 dex will lead to a decrease in effective temperature for early-type M dwarfs of ~ 100 K. Applying this result to our high resolution modeling results and assuming a gravity deficiency of $\Delta \log g \sim 1.0$ dex leads to an adjusted effective temperature of $T_{\text{eff}} \sim 3300$ K for GJ 436. This result is in agreement with the effective temperature derived with surface gravity fixed to $\log g = 5.0$ dex; in that case, we found $T_{\text{eff}} \sim 3400$ K (see column 6 of Table 2).

3.3. Low Resolution Modeling

We also modeled a low resolution red spectrum of GJ 436 kindly provided by D. Kirkpatrick. This spectrum was taken on 3 December 1995 using the red channel of the double spectrograph with the 158 line mm^{-1} grating on the Hale 5 m telescope with an integration time of 5 sec. It extends from 5140-9176 Å and the resolution is $R = 1140$, corresponding to an instrumental profile having a FWHM of 7 Å. To compare the observed spectrum to the models, the spectra were cross-correlated and matched in resolution in the same way as was done for the high resolution spectra. Because the individual molecular lines are not resolved at this resolution, the full spectrum was used in the fit.

The low resolution modeling of GJ 436 yielded $T_{\text{eff}} = 3500$ K, $\log g = 5.0$, and $[M/H] = 0.0$. This result is somewhat different from the result obtained from our high resolution spectrum that gave $T_{\text{eff}} = 3200$ K, $\log g = 4.0$, and $[M/H] = 0.0$. Figure 2 provides a comparison at low resolution of the best fit high resolution model to the best fit low resolution model. The discrepancy between the results obtained at high resolution versus low resolution is not surprising, as the high resolution modeling is sensitive to strengths of the atomic lines, which are influenced by the oscillator strengths of the TiO lines. In contrast, the low resolution modeling is sensitive to the shape of the continuum dictated by the gross structure of the TiO bands. It is interesting to note that for the three stars in our sample that have been modeled at low resolution (GJ 436, GJ 411, and GJ 908), the

derived effective temperatures are consistently higher than those derived at high resolution when surface gravity is left as a free parameter. On the other hand, when surface gravity is fixed to a reasonable value of $\log g = 5.0$, the high and low resolution results come into good agreement (see Table 2).

However, due to the inaccuracies in the TiO line list revealed by the high resolution spectra, it is likely that the continua in the model spectra carry significant errors at both low and high resolution. Therefore, while the fits at low and high resolution come into good agreement when the surface gravities are fixed to the same value, the derived parameters may still be systematically in error. For future work in this area, an important distinction between modeling at high resolution versus that at low resolution is that at high resolution, errors in the continuous opacity due to the poorly determined TiO lines can be directly observed in the TiO lines themselves. At low resolution, errors in the TiO opacity are not as directly obvious. High resolution observational spectra are therefore required to test new models that incorporate adjustments to the molecular continuous opacity. We note that while the current TiO line list and corresponding oscillator strengths have been adjusted and improved in the last decade, molecular opacities remain the primary source of uncertainty in model synthetic spectra of M dwarf atmospheres (Valenti et al. 1998, Allard et al. 2000, Bean et al. 2006). The accuracy of derived parameters at the moment appears to be largely dependent on the observed spectral region. Valenti et al. (1998) and Bean et al. (2006), for example, have improved portions of the M dwarf models by deriving wavelengths and oscillator strengths of the TiO lines from the M dwarfs themselves. As a result of this effort, Bean et al. (2006) showed that careful treatment of specific TiO bandheads can lead to improved synthesis of the spectra of those lines. However, in the absence of observations containing these carefully tuned regions, stellar parameters derived directly from synthetic spectra remain highly uncertain. The TiO opacities for the PHOENIX models continue to be revised and tested, and improved opacities will likely be incorporated into the next set of available grids (Allard et al., in prep). It would be valuable if these new grids were tested using a sizable sample of M dwarf spectra at high resolution, as it is likely that uncertainties in the TiO opacity have led to biases in the currently-accepted M dwarf temperature scale. For the present purposes of characterizing GJ 436, however, we tentatively assign an effective temperature that is the simple average of our low and high resolution results: $T_{\text{eff}} \sim 3350 \pm 300$ K.

4. Doppler Measurements and New Orbital Model for GJ 436b

We have obtained 59 spectra of GJ 436 at the Keck 1 telescope with the HIRES echelle spectrometer (Vogt et al. 1994) during the 6.5-year period, Jan 2000 to July 2006 (JD = 2451552-2453934). These velocities include 17 new, unpublished measurements made during the past two seasons since announcement of the planet, GJ 436b (Butler et al. 2004). In addition, we remeasured the Doppler shifts of all past spectra using a newly improved Doppler analysis pipeline that includes a filter for the telluric absorption lines and a superior

template spectrum for spectral modeling. The exposure times were typically 8 min yielding $S/N \approx 150$ and resulting in an uncertainty in the radial velocity of 2.6 m s^{-1} (median) per exposure.

The times of all observations, the velocities, and the uncertainties are listed in Table 4. Effects due to secular acceleration have been calculated and removed from the listed velocities. The uncertainties consist of internal errors only, based on the uncertainty in the mean Doppler shift of all ~ 700 spectral segments. Occasionally we obtained two or three consecutive spectra within a 30 minute interval from which we computed the weighted average velocity and the correspondingly reduced uncertainty. Figure 3 shows all of the measured velocities vs. time for GJ 436.

We attempted to fit the velocities for GJ 436 with several orbital models shown in Figures 4-6. A circular orbit fit to the velocities, shown in Figure 4, yields residuals correlated in phase and a large value of $\sqrt{\chi^2_\nu} = 2.04$. This fit is unacceptable, and we carry out a statistical assessment of it in section §5. A full Keplerian model, with the eccentricity allowed to float, produced a superior fit, as shown in Figure 5. This model yields residuals with $\text{RMS} = 4.76 \text{ m s}^{-1}$ and $\sqrt{\chi^2_\nu} = 1.69$, both considerably smaller than the circular orbit. The best-fit parameters from this Keplerian model were $P = 2.6439 \text{ d}$, $e = 0.185$, $K = 18.25 \text{ m s}^{-1}$. Adopting the (revised) stellar mass of $0.44 M_\odot$ implies a minimum mass for the planet of $M \sin i = 0.0706 M_{\text{JUP}} = 22.4 M_{\text{Earth}}$ and a semi-major axis of 0.0285 AU .

The linear trend in the velocities evident in Figure 3 motivated a final model that combines both a Keplerian orbit and a linear trend in the velocities, presumably caused by a more distant orbiting companion. A least-squares fit to the velocities gave residuals with $\text{RMS} = 4.27 \text{ m s}^{-1}$, $\sqrt{\chi^2_\nu} = 1.57$, both superior to (lower than) those from the Keplerian model without a trend. (The additional free parameter for the trend was suitably included in both statistics.) This model with the trend gave orbital parameters, $P = 2.64385 \pm 0.00009 \text{ d}$, $e = 0.160 \pm 0.019$, $K = 18.34 \pm 0.52 \text{ m s}^{-1}$, and a linear velocity slope of 1.36 m s^{-1} per year. All orbital parameters are listed in Table 5, and they are not greatly different from those obtained with no linear trend. The new orbital parameters are only slightly different from those in Butler et al. (2004) who found $P = 2.6441 \text{ d}$, $K = 18.1 \text{ m s}^{-1}$, $e = 0.12$. But the current linear trend of 1.36 m s^{-1} per year is smaller than that found by Butler et al. (2004): 2.7 m s^{-1} per year. The modest reduction in RMS and $\sqrt{\chi^2_\nu}$ warrants an assessment of the reality of the trend, provided in §5.

We carried out all Keplerian fits by assigning weights to each Doppler measurement that are the inverse of the quadrature sum of the internal velocity errors and the estimated jitter, 1.9 m s^{-1} for similar M dwarfs, based on the velocity RMS of stable M dwarfs. The best-fit orbital parameters are very weakly dependent on the precise value of jitter.

The model that includes a Keplerian with a linear trend yields the most likely physical parameters for the planet. Adopting the (revised) stellar mass of $0.44 M_\odot$, the best-fit model implies a minimum mass for the orbiting companion of $M \sin i = 0.0713 M_{\text{JUP}} = 22.6 M_{\text{Earth}}$ and a semi-major axis of 0.0285 AU . We note that the value of $M \sin i$ found

here is higher than that ($0.067 M_{\text{JUP}}$) reported by Butler et al. (2004) due primarily to the 7% higher stellar mass adopted. However, the improvements to the Doppler analysis have reduced the RMS of the velocity residuals to the fit from 5.3 m s^{-1} to 4.3 m s^{-1} .

The non-zero eccentricity of $e=0.16\pm 0.02$ is somewhat surprising. Among the 23 exoplanets with periods under 4 d, this eccentricity is the highest (Butler et al. 2006), and only one other planet may have an eccentricity as high as 0.10. Tidal circularization is thought to be responsible for the nearly circular orbits of the short period planets. If so, the high orbital eccentricity of this close-in, Neptune-mass planet poses a mystery about its origin. Two possible resolutions are that a more distant planet pumps its eccentricity or that the tidal Q value is high enough to avoid tidal circularization during the 3-10 Gyr age of this system.

5. Orbital Constraints on GJ 436b

Given the short orbital period of GJ 436b, a detection of a non-zero eccentricity can carry implications for eccentricity evolution in this system. In this section, we evaluate the observational evidence for the planet’s non-zero eccentricity and the presence of a long-term trend in the radial velocity data. Because the eccentricity of a bound orbit must lie between zero and unity, the best-fit orbit for systems with small orbital eccentricities will suffer from a systematic Lutz-Kelker bias toward larger eccentricities. As noted in §4, the best-fit orbital solution has an eccentricity of $e = 0.160$ and bootstrap-style resampling suggests an uncertainty of order 0.019. Unfortunately, the error estimates derived from bootstrap-style resampling can significantly underestimate the true uncertainties in orbital parameters, as demonstrated by comparisons with Bayesian analyses (Ford 2005; Gregory 2005). Modern computers and advanced statistical algorithms make it practical to replace this type of frequentist analysis with a statistically rigorous Bayesian analysis. We perform a Bayesian analysis to determine the posterior probability density function (posterior PDF) for the Keplerian orbital elements, assuming the observed radial velocity variations are due to a single planet on a Keplerian orbit. We assume a prior PDF that is the product of prior PDFs for each of the model parameters individually. We assign prior PDFs as follows: $p(P) \sim 1/P$ for $P_{\text{min}} \leq P \leq P_{\text{max}}$ for the orbital period, $p(K) \sim 1/(K_o + K)$ for $K \leq K_{\text{max}}$ for the velocity semi-amplitude, $p(e) \sim 1$ for $0 \leq e < 1$ for the orbital eccentricity, $p(\omega) = 1/2\pi$ for $0 \leq \omega < 2\pi$ for the argument of pericenter, $p(M_0) = 1/2\pi$ for the mean anomaly at a specified epoch, $p(C) \sim 1$ for the mean stellar velocity, and $p(\sigma_j) \sim 1/(\sigma_o + \sigma_j)$ for $\sigma_j \leq \sigma_{\text{max}}$ for the stellar jitter. In some simulations where we also include a linear velocity trend, D , we have assumed a prior PDF uniform in slope, $p(D) = 1/2D_{\text{max}}$ for $-D_{\text{max}} \leq D \leq D_{\text{max}}$. We choose the constants $P_{\text{min}} = 1 \text{ d}$, $P_{\text{max}} = 6.3 \text{ yr}$, $K_{\text{max}} = 2.8 \text{ km s}^{-1}$, $\sigma_{\text{max}} = 2.8 \text{ km s}^{-1}$, $K_o = \sigma_o = 1 \text{ m s}^{-1}$, and $D_{\text{max}} = 10 \text{ m s}^{-1}$ per yr, so that the corresponding priors can be properly normalized. We assume that the stellar jitter is Gaussian and uncorrelated, and we add it in quadrature with the observational uncertainty for each observation ($\sigma_i = \sqrt{\sigma_{\text{obs},i}^2 + \sigma_j^2}$).

The likelihood (the probability of making the actual observations for a given set of model parameters) is computed as the product of independent Gaussians with mean $v_{\text{obs},i}$ and standard deviation σ_i , at each time t_i , using the actual observation times, observed velocities, and uncertainties in Table 5. We sample from the posterior PDF using the numerical techniques of Markov chain Monte Carlo (Ford 2005, 2006; Gregory 2005). Fig. 7 (upper panel) shows the posterior probability distribution marginalized over all model parameters except the orbital eccentricity. When we include a linear slope (solid line), there is only a 5% posterior probability that the eccentricity is less than 0.068 and a 0.1% posterior probability that the eccentricity is less than 0.004, *if we assume a uniform prior for eccentricity*. Similarly, Fig. 7 (lower panel) shows the posterior probability distribution marginalized over all model parameters except the slope. When we allow for an eccentric orbit for GJ 436b (solid line), there is a 99.8% posterior probability that the linear slope is positive, *if we assume a uniform prior for the velocity slope*.

The above analyses do not directly address the question of whether the radial velocity observations provide evidence for a non-zero eccentricity and/or non-zero linear slope. To address these questions, we must consider four sets of models: one set of models with a planet on a circular orbit and no slope (\mathcal{M}_{cn}), one set of models with a planet on an eccentric orbit and no slope (\mathcal{M}_{en}), one set of models with a planet on a circular orbit and a linear slope (\mathcal{M}_{cs}), and one set of models with a planet on an eccentric orbit and a linear slope (\mathcal{M}_{es}). Since the \mathcal{M}_{es} models have three more model parameters than the models in \mathcal{M}_{cn} , we should expect that some models from \mathcal{M}_{es} will provide better fits to the observations than the best models from \mathcal{M}_{cn} , even if the planet were actually on a circular orbit. Bayesian model selection naturally provides a framework for quantifying the ‘‘Occam’s razor’’ factor that determines how much better the more complex model must fit to justify adding the extra model parameters. We construct a composite model (\mathcal{M}) that includes a discrete indicator variable that specifies whether to use model \mathcal{M}_{cn} , \mathcal{M}_{cs} , \mathcal{M}_{en} , or \mathcal{M}_{es} . We assume prior probabilities for each of these models, $p_{cn} = p_{en} = p_{cs} = p_{es} = 0.25$.

To determine the posterior probability for an eccentric orbit, we must compute the posterior probability PDF marginalized over all parameters except the index specifying the model. Unfortunately, the standard MCMC techniques (e.g., Ford 2005, 2006) allow us to sample from the posterior PDF assuming any one of these models, but do not provide the normalizations. We have used additional simulation techniques to evaluate the ratio of the normalizations of each pair of these models. A detailed description of the various algorithms and the advantages and disadvantages of each will be presented in a subsequent paper (Ford et al. 2006, in prep). Here, we describe only one of the more conceptually simple algorithms. We estimate the necessary integrals with regular Monte Carlo integration, but limit the range of integration to the small volume of parameter space that dominates the contribution to the marginalized posterior probability (as determined from the MCMC simulations).

Our Monte Carlo integration reveals the model with both an eccentricity and a linear slope is strongly favored (by a factor of $\simeq 10^{10}$) over the model with a circular orbit and no

slope. If we assume there is a linear slope, then the eccentric model is $\simeq 200$ times more likely than the circular model. Similarly, if we assume an eccentric model, then the model with a linear slope is $\simeq 10^4$ times more likely than the model without a slope. *Therefore, we conclude that the radial velocity observations provide strong evidence for both a non-zero eccentricity and a non-zero linear velocity trend.*

6. Discussion

The revised mass for the star GJ 436 of $0.44 M_{\odot}$ and the revised orbital parameters and $M \sin i$ for the planet have tightened the constraints on the structure of this planetary system. The minimum mass of the planet remains slightly greater than that of Neptune with $M \sin i = 22.6 M_{\text{Earth}}$ and orbiting with semimajor axis, $a = 0.0285 \text{ AU}$.

Two new results have emerged from the present analysis that render the system interesting and puzzling. The eccentricity is definitely non-zero, with $e = 0.16 \pm 0.02$, the highest eccentricity for any exoplanet with an orbital period less than 4 d. It has apparently avoided tidal circularization. Moreover, the velocities exhibit a linear trend of 1.3 m s^{-1} per year that appears to be real, indicating the presence of a more distant companion, the mass and orbit of which remain poorly constrained. It is tempting to suppose that this outer companion is responsible for pumping the eccentricity of the inner planet.

Two scenarios seems possible. In the first scenario, planet b resides in an eccentric orbit and the linear velocity slope is due to a companion so far away that it isn't exciting the eccentricity of planet b. In this case, tidal theory would argue for a not-low value of Q and hence against a rocky planet. Scaling the Earth's $Q \sim 300$ by the forcing period and scaling the Earth's radius by $22^{1/3}$, one gets a tidal circularization time of 2 million years, not consistent with the age of the star that is certainly several billion years. It shows no signs of youth such as rapid rotation, or enhanced magnetic, chromospheric and coronal activity.

If one scales Neptune's Q value, $Q \sim 10^5$, by the forcing period and uses its radius, then the tidal circularization time is $2 \times 10^9 \text{ yr}$. If the planet started on an eccentric orbit, then this timescale is plausible, as the orbit will have only partially circularized. The Q estimates for the ice giants in the solar system range from 10^4 to a few 10^6 . Such values provide an interesting constraint on Q for a hot-Neptune.

In a second scenario, the planet b resides on an eccentric orbit, but the slope is due to a planet or binary star that comes close enough to pump the planet's eccentricity despite the tidal damping. In this case, planet b can be terrestrial or an ice giant since it is continually being pumped.

But one wonders if such pumping is consistent with the velocity data. If we naively approximate the outer "planet c" to be on a circular orbit, then $m_c \sin i \sim 0.2 M_{\text{JUP}}$ ($P/20 \text{ yr}$)^{4/3} (slope / 1.25 m/s/yr), where a 20 yr minimum orbital time scale comes from ~ 4

times the duration of observations. Even if we take the duration of observations to be the minimum orbital period for planet c, then the ratio of semimajor axes is at least ~ 100 . With such large separation, the outer planet is unlikely to be effective at exciting an eccentricity.

To test this, we have performed numerical integrations in the secular octupole approximation (averaging over orbits and expanding in terms of ratio of semi-major axes, but not eccentricities, inclinations, or mass ratios). We assume that this approximation gives a rough estimate of the mass of an outer planet in a coplanar system with $\sin i = 1$. For an outer planet orbital period less than 14 years (and hence masses less than $0.12 M_{\text{JUP}}$), the outer planet would need an eccentricity larger than 0.5 to be able to induce an eccentricity of 0.16 for planet b. Alternatively, an outer planet with orbital period of 25 years (and hence a mass of $\sim 0.27 M_{\text{JUP}}$) would need an eccentricity of only 0.2 to be able to induce the observed eccentricity of GJ 436b. The timescale for the secular eccentricity perturbations is less than 10^6 yr. So this configuration would maintain the observed eccentricity of GJ 436b, regardless of the assumed composition and value of the tidal Q . Given that we observe both an eccentricity and a slope, this scenario offers a reasonable explanation. Doppler observations during the upcoming years may reveal the mass and period of the outer planet, if it exists.

The authors are grateful to D. Kirkpatrick for supplying the low resolution spectrum of GJ 436 used in this paper. H.M. is also grateful to D. Fischer and R. Foley for their help on this project and to the Graduate Research Fellowship Program at NSF for funding this research. E.B.F. acknowledges the support of the Miller Institute for Basic Research. We appreciate support by NASA grant NAG5-75005 and by NSF grant AST-0307493 (to SSV); support by NSF grant AST-9988087, by NASA grant NAG5-12182 and travel support from the Carnegie Institution of Washington (to RPB). We thank NASA and the University of California for allocations of Keck telescope time toward the planet search around M dwarfs. This research has made use of the Simbad database, operated at CDS, Strasbourg, France. Finally, the authors wish to extend thanks to those of Hawaiian ancestry on whose sacred mountain of Mauna Kea we are privileged to be guests. Without their generous hospitality, the Keck observations presented herein would not have been possible.

REFERENCES

- Alibert, Y., Mordasini, C., Benz, W., & Winisdoerffer, C. 2005, *A&A*, 434, 343–353
- Allard, F., Hauschildt, P. H., & Schwenke, D. 2000, *ApJ*, 540, 1005
- Allard, F., Hauschildt, P. H., Alexander, D. R., Tamanai, A., & Schweitzer, A. 2001, *ApJ*, 556, 357
- Baraffe, I., Chabrier, G., Allard, F., & Hauschildt, P. H. 1998, *A&A*, 337, 403
- Basri, G., Mohanty, S., Allard, F., Hauschildt, P. H., Delfosse, X., Martín, E. L., Forveille, T., & Goldman, B. 2000, *ApJ*, 538, 363
- Bean, J. L., Sneden, C., Hauschildt, P. H., Johns-Krull, C. M., & Benedict, G. F. 2006, *ArXiv Astrophysics e-prints*, arXiv:astro-ph/0608093
- Beaulieu, J.-P., et al. 2006, *Nature*, 439, 437
- Benedict, G. F., et al. 2001, *AJ*, 121, 1607
- Bond, I. A., et al. 2004, *ApJ*, 606, L155
- Bonfils, X., Delfosse, X., Udry, S., Santos, N. C., Forveille, T., & Ségransan, D. 2005, *A&A*, 442, 635
- Bonfils, X., et al. 2005, *A&A*, 443, L15
- Boss, A. P. 2006, *ApJ*, 644, L79
- Butler, R.P., Marcy, G.W., Williams, E., McCarthy, C., Dosanjuh, P., & Vogt, S.S. 1996, *PASP*, 108, 500
- Butler, R. P., Vogt, S. S., Marcy, G. W., Fischer, D. A., Wright, J. T., Henry, G. W., Laughlin, G., & Lissauer, J. J. 2004, *ApJ*, 617, 580
- Butler, R. P., et al. 2006, *ApJ*, 646, 505
- Buzzoni, A., Chavez, M., Malagnini, M. L., & Morossi, C. 2001, *PASP*, 113, 1365
- Cumming, A. 2004 *MNRAS*, 354, 1165.
- D’Antona, F. & Mazzitelli, I. 1994, *ApJS*, 90, 467
- Delfosse, X., Forveille, T., Perrier, C., & Mayor, M. 1998, *A&A*, 331, 581
- Delfosse, X., Forveille, T., Ségransan, D., Beuzit, J.-L., Udry, S., Perrier, C., & Mayor, M. 2000, *A&A*, 364, 217

- Endl, M., Cochran, W. D., Kürster, M., Paulson, D. B., Wittenmyer, R. A., MacQueen, P. J., & Tull, R. G. 2006, *ApJ*, 649, 436
- Ford, E.B. 2005, *AJ*, 129, 1706.
- Ford, E. B. 2006, *ApJ*, 642, 505
- Goldreich, P., Lithwick, Y., & Sari, R. 2004, *ARA&A*, 42, 549
- Gould, A., et al. 2006, *ApJ*, 644, L37
- Gregory, P.C. 2005 *ApJ* 631, 1198.
- Hauschildt, P. H., Allard, F., & Baron, E. 1999, *ApJ*, 512, 377
- Henry, T. J. & McCarthy, D. W. 1993, *AJ*, 106, 773
- Hubickyj, O., Bodenheimer, P., & Lissauer, J. J. 2004, *Revista Mexicana de Astronomia y Astrofisica Conference Series*, 22, 83
- Ida, S., & Lin, D. N. C. 2005, *ApJ*, 626, 1045
- Jones, H. R. A., Longmore, A. J., Jameson, R. F., & Mountain, C. M. 1994, *MNRAS*, 267, 413
- Jones, H. R. A., Longmore, A. J., Allard, F., & Hauschildt, P. H. 1996, *MNRAS*, 280, 77
- Kirkpatrick, J. D., Kelly, D. M., Rieke, G. H., Liebert, J., Allard, F., & Wehrse, R. 1993, *ApJ*, 402, 643
- Laughlin, G., Bodenheimer, P., & Adams, F. C. 2004, *ApJ*, 612, L73
- Leggett, S. K. 1992, *ApJS*, 82, 351
- Leggett, S. K., Allard, F., Berriman, G., Dahn, C. C., & Hauschildt, P. H. 1996, *ApJS*, 104, 117
- Leggett, S. K., Allard, F., Dahn, C., Hauschildt, P. H., Kerr, T. H., & Rayner, J. 2000, *ApJ*, 535, 965
- Leggett, S. K., Allard, F., Geballe, T. R., Hauschildt, P. H., & Schweitzer, A. 2001, *ApJ*, 548, 908
- Leggett, S. K., Hauschildt, P. H., Allard, F., Geballe, T. R., & Baron, E. 2002, *MNRAS*, 332, 78
- Perryman, M. A. C., et al. 1997, *A&A*, 323, L49

Reid, N. & Hawley, S. L. 2000, *New light on dark stars : red dwarfs, low mass stars, brown dwarfs* / Neill Reid and Suzanne L. Hawley. New York : Springer, 2000. (Springer-Praxis series in astronomy and astrophysics)

Rivera, E. J., et al. 2005, *ApJ*, 634, 625

Siess, L., Dufour, E., & Forestini, M. 2000, *A&A*, 358, 593

Thommes, E. W., Duncan, M. J., & Levison, H. F. 2002, *AJ*, 123, 2862

Udalski, A., et al. 2005, *ApJ*, 628, L109

Valenti, J. A., Piskunov, N., & Johns-Krull, C. M. 1998, *ApJ*, 498, 851

Veeder, G. J. 1974, *AJ*, 79, 1056

Vogt, S. S. et al. 1994. *Proc. Soc. Photo-Opt. Instr. Eng.*, 2198, 362.

Table 1. Metallicities (Bonfils et al. 2005a)

Star	[M/H]
GJ 436	-0.03
GJ 411	-0.42
GJ 424	-0.48
GJ 752A	-0.05
GJ 860A	-0.02
GJ 908	-0.53

Table 2. Summary of Effective Temperature Results

Object	Spec. T.	T_{eff} Low res. (K)	T_{eff} Echelle (by eye) (K)	T_{eff} Echelle (num.) (K)	T_{eff} Echelle (log g = 5.0, fixed) (K)
GJ 436	M2.5	3500	3200	3200	3400
GJ 411	M2	>3500, 3500, 4000*	3400	3370	3630
GJ 424	M0	-	3400	3550	3830
GJ 752A	M2.5	-	3300	3240	3430
GJ 860A	M3	-	3200	3140	3380
GJ 908	M1	3700 ⁺	3500	3530	3790

*Derived by Kirkpatrick (1993), Leggett et al. (1996), and Jones et al. (1996), respectively.

⁺Derived by Leggett et al. (1996)

Table 3. Summary of Surface Gravity Results

Object	Spec. T.	log g Low res. (dex)	log g Echelle (by eye) (dex)	log g Echelle (num.) (dex)
GJ 436	M2.5	5.0	4.0	4.0
GJ 411	M2	5.0*	4.5	4.3
GJ 424	M0	-	4.0	4.2
GJ 752A	M2.5	-	4.5	4.0
GJ 860A	M3	-	4.0	4.0
GJ 908	M1	-	4.5	4.4

*Derived by Jones et al. (1996)

Table 4. Radial Velocities for GJ 436

JD -2440000	RV (m s ⁻¹)	Unc. (m s ⁻¹)
11552.077	5.84	2.3
11583.948	0.67	2.0
11706.865	-12.05	2.6
11983.015	9.48	2.8
12064.871	12.76	2.9
12308.084	19.86	2.5
12333.038	-26.89	3.4
12334.054	17.15	2.4
12334.935	-1.45	2.7
12363.039	13.43	2.9
12681.057	11.36	2.9
12711.898	0.00	2.4
12712.902	5.14	2.7
12804.878	18.86	2.6
12805.829	-7.21	2.4
12828.800	14.85	2.5
12832.758	-21.88	2.4
12833.763	13.01	2.4
12834.779	-3.56	3.0
12848.752	-21.18	2.6
12849.762	17.95	2.1
12850.764	-3.77	2.1
12988.146	-6.43	1.2
12989.146	-16.33	1.8
13015.141	-13.13	1.5
13016.073	11.10	1.5
13017.046	2.74	1.6
13018.142	-7.65	1.8
13044.113	-18.32	1.5
13045.018	-1.57	1.5
13045.985	6.91	1.4
13069.032	14.71	1.5
13073.991	-0.89	1.9
13077.066	16.30	2.7
13153.817	22.57	2.0
13179.759	-4.15	2.6

Table 4—Continued

JD -2440000	RV (m s ⁻¹)	Unc. (m s ⁻¹)
13180.803	8.51	2.3
13181.746	-11.20	2.0
13189.787	-20.17	1.7
13190.754	12.47	1.8
13195.767	0.19	1.7
13196.772	-7.03	2.0
13339.140	26.74	2.5
13340.129	-6.55	2.2
13370.133	4.71	2.9
13401.055	-12.44	2.5
13483.876	4.43	2.4
13693.112	18.49	2.2
13695.138	-3.55	1.8
13724.143	-1.82	2.8
13725.120	21.84	2.6
13748.059	3.06	2.4
13753.075	-7.75	2.4
13754.040	28.81	2.6
13776.052	-8.42	2.2
13777.023	-10.13	2.2
13807.020	21.15	2.5
13841.887	6.84	2.3
13933.781	23.54	2.6

Table 5. Orbital Parameters for GJ 436

Parameter	
P (d)	2.64385 (0.00009)
T_p (JD)	2451551.716 (0.01)
e	0.160 (0.019)
ω (deg)	351 (1.2)
K_1 (m s ⁻¹)	18.34 (0.52)
$f_1(m)$ (M _⊙)	1.6258e-12
a_{rel} (AU)	0.0285
$M \sin i$ (M _{Jup})	0.0713 (0.006)
dv/dt (m s ⁻¹ per yr)	1.36 (0.4)
Nobs	59
RMS (m s ⁻¹)	4.27
$\sqrt{\chi^2_\nu}$	1.57

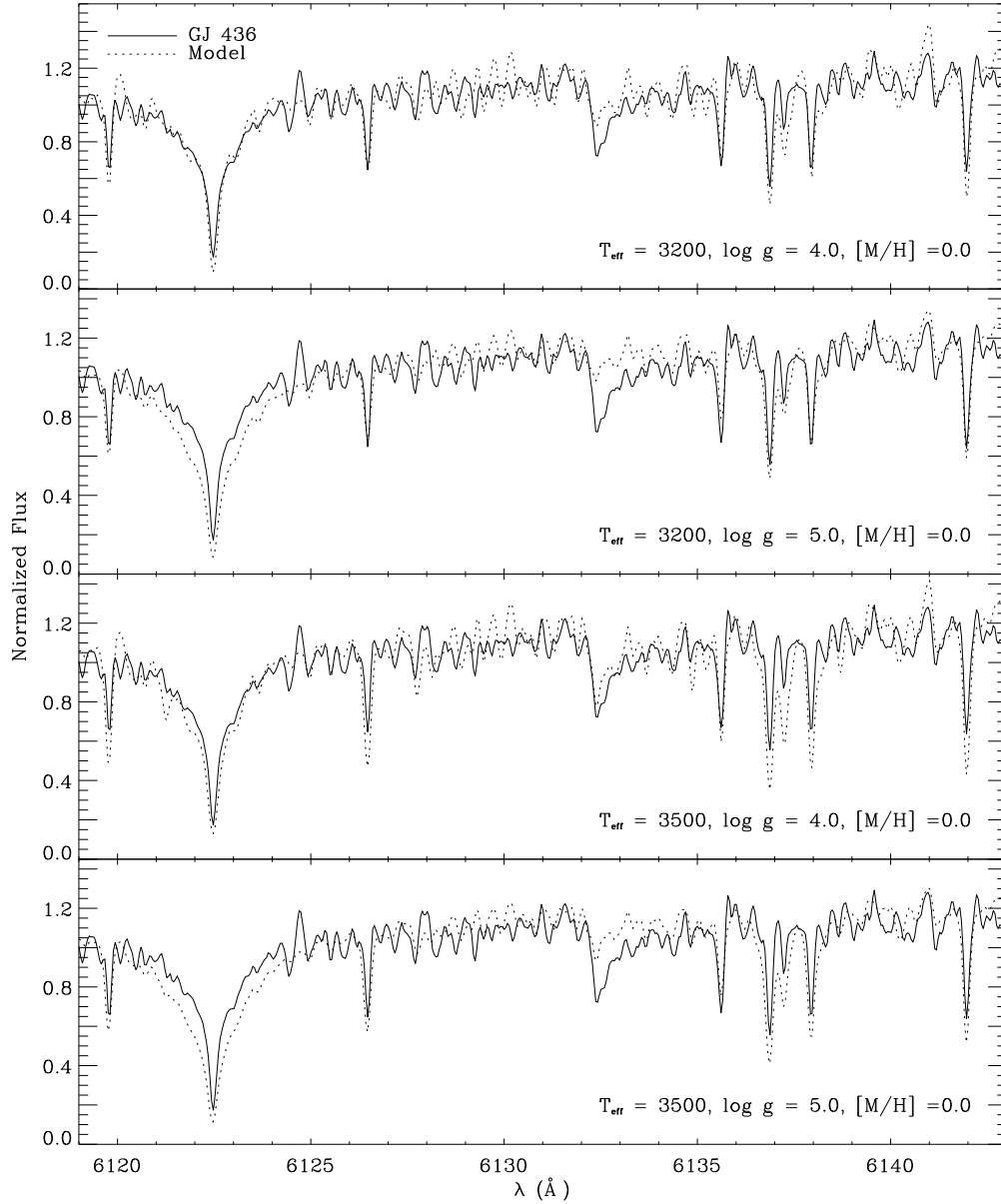


Fig. 1.— Comparison at high resolution of the high resolution best fit and the low resolution best fit for GJ 436. The figures show a representative portion of one echelle order; notice that in all figures, the model TiO molecular lines do not match the observed lines. The top panel shows the best fit at this resolution. However, while the atomic line profiles are well fit, and the overall strength of the TiO lines is similar, the surface gravity for this model is unphysical (see the text). When the surface gravity is fixed to a reasonable value (panels 2 and 4), the overall strength of the molecular lines and the atomic line profiles can not be simultaneously matched.

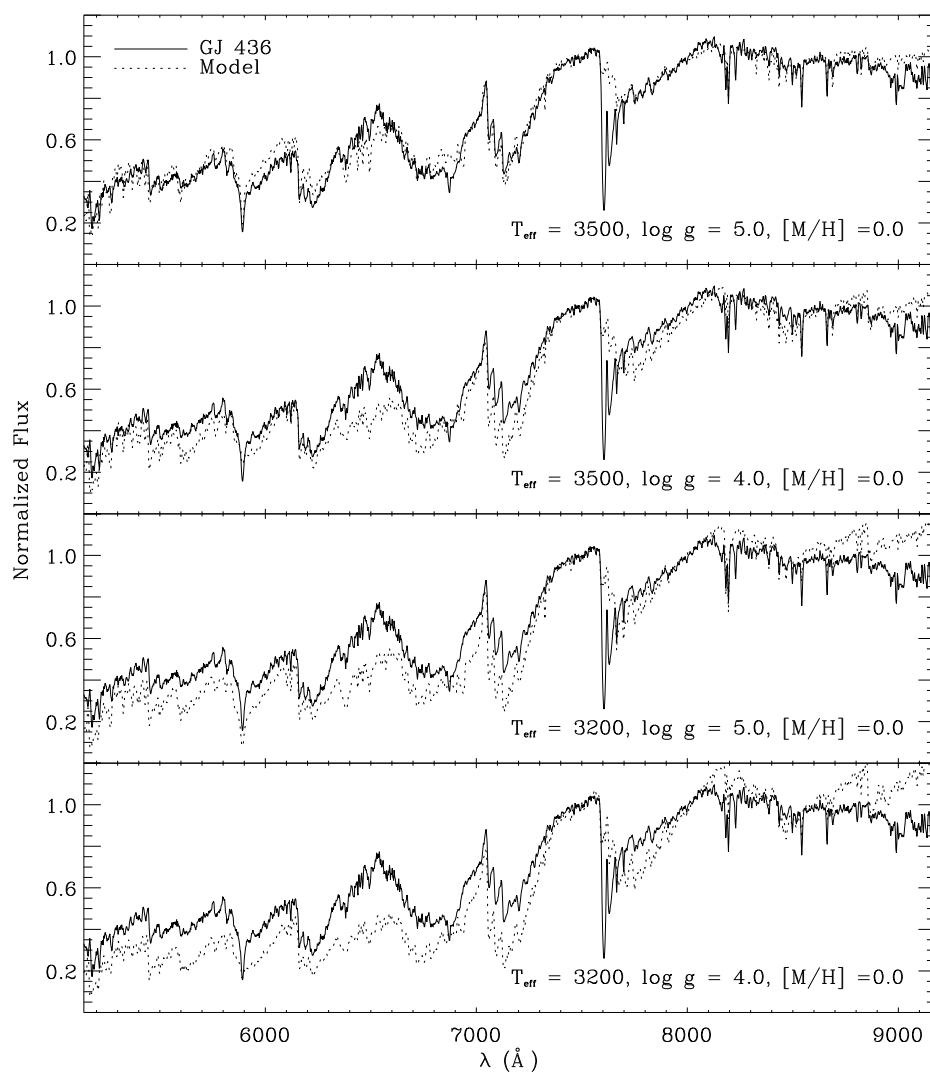


Fig. 2.— Comparison, at low resolution, of the high resolution best fit and the low resolution best fit for GJ 436. The top panel shows the best fit to the low resolution spectrum, while the bottom panel shows the high resolution best fit model. Note that at low resolution, errors in the continuum introduced by the poorly determined TiO lines cannot be directly observed, in contrast to the situation at high resolution (see Figure 1).

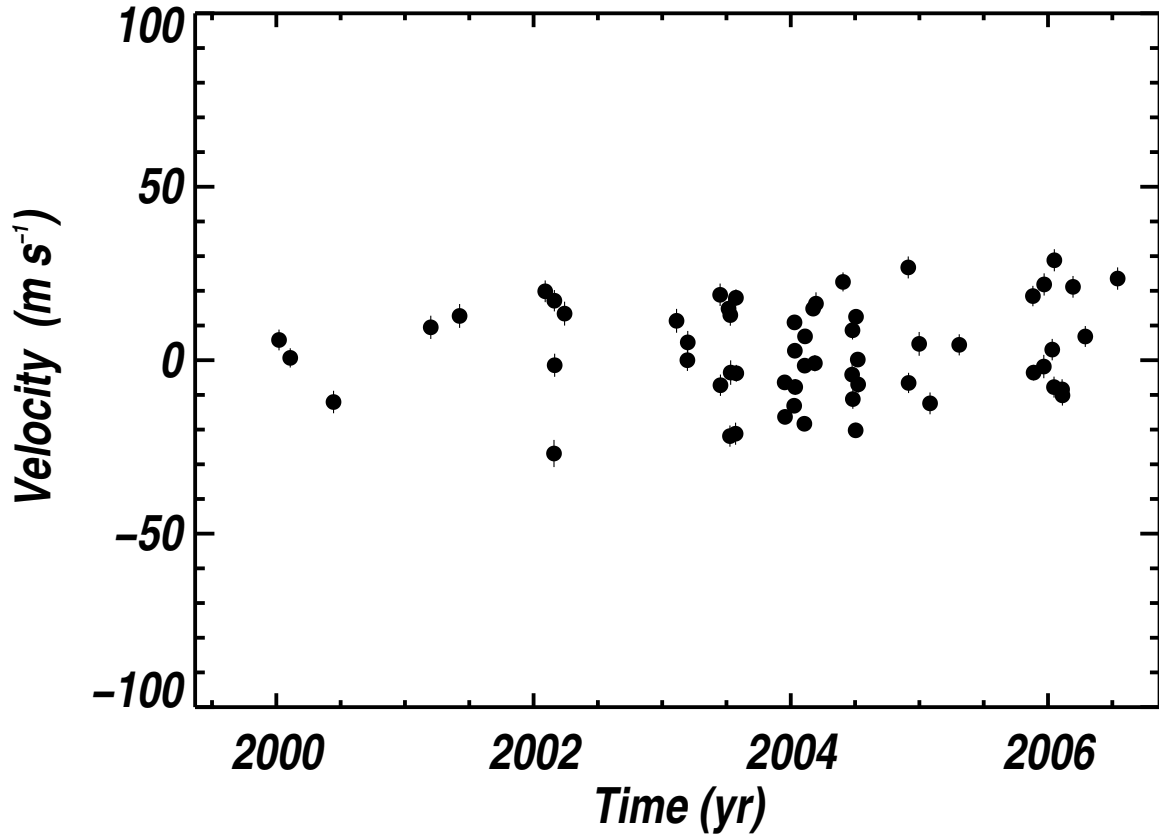


Fig. 3.— Measured velocities vs. time for GJ 436. The RMS scatter of $\sim 13.5 \text{ m s}^{-1}$ is greater than the uncertainties ($\sim 4 \text{ m s}^{-1}$) shown as error bars, indicating real variation in velocity. There is a hint of an upward trend in the velocities. The error bars show the quadrature sum of the internal errors (median 2.6 m s^{-1}) and jitter (1.9 m s^{-1}).

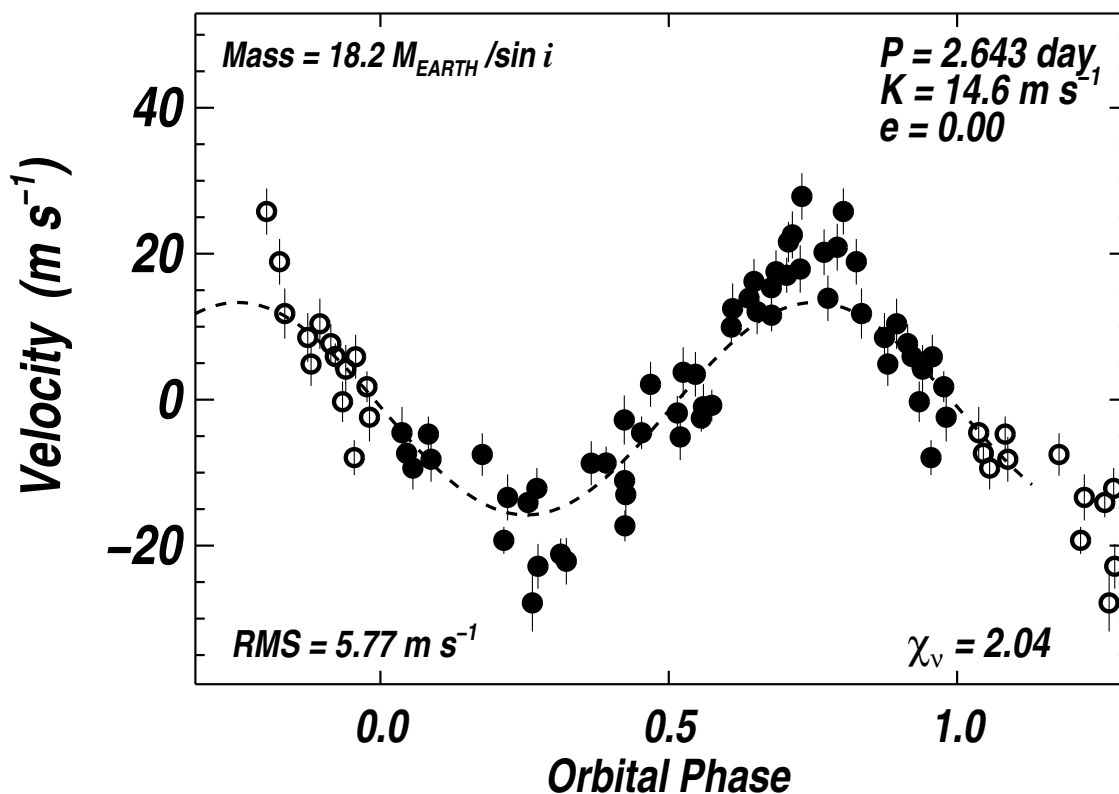


Fig. 4.— Circular orbit fit (dashed line) to measured velocities (filled dots) vs. orbital phase for GJ 436. Repeated points outside phases 0 to 1 are shown as open circles. The resulting parameters are: $P = 2.644 \text{ d}$, $M \sin i = 0.057 M_{JUP} = 18.1 M_{Earth}$. No velocity trend was added to the Keplerian model. The RMS of the residuals to this fit is 5.77 m s^{-1} and reduced $\sqrt{\chi_v^2} = 2.04$, clearly inferior to models with non-zero eccentricity (Fig. 5, Fig. 6).

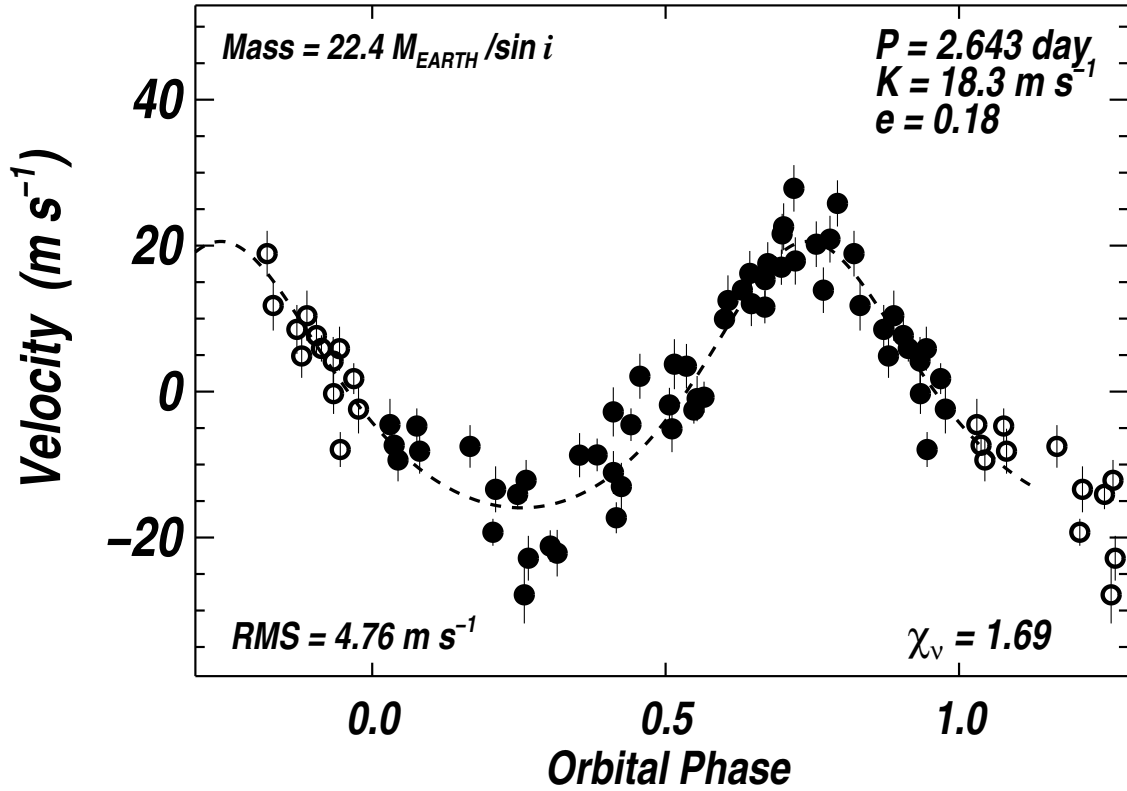


Fig. 5.— Full Keplerian model fit (dashed line) to measured velocities (dots) vs. orbital phase for GJ 436, with repeated points (outside phases 0–1) shown as open circles. $P = 2.6439$ d, $e = 0.18$, $M \sin i = 0.0706 M_{\text{JUP}} = 22.4 M_{\text{Earth}}$. No velocity trend was added to the Keplerian model. The RMS of the residuals to this fit is 4.76 m s^{-1} with a reduced $\sqrt{\chi^2_{\nu}} = 1.69$. The uncertainties include internal errors and jitter added in quadrature.

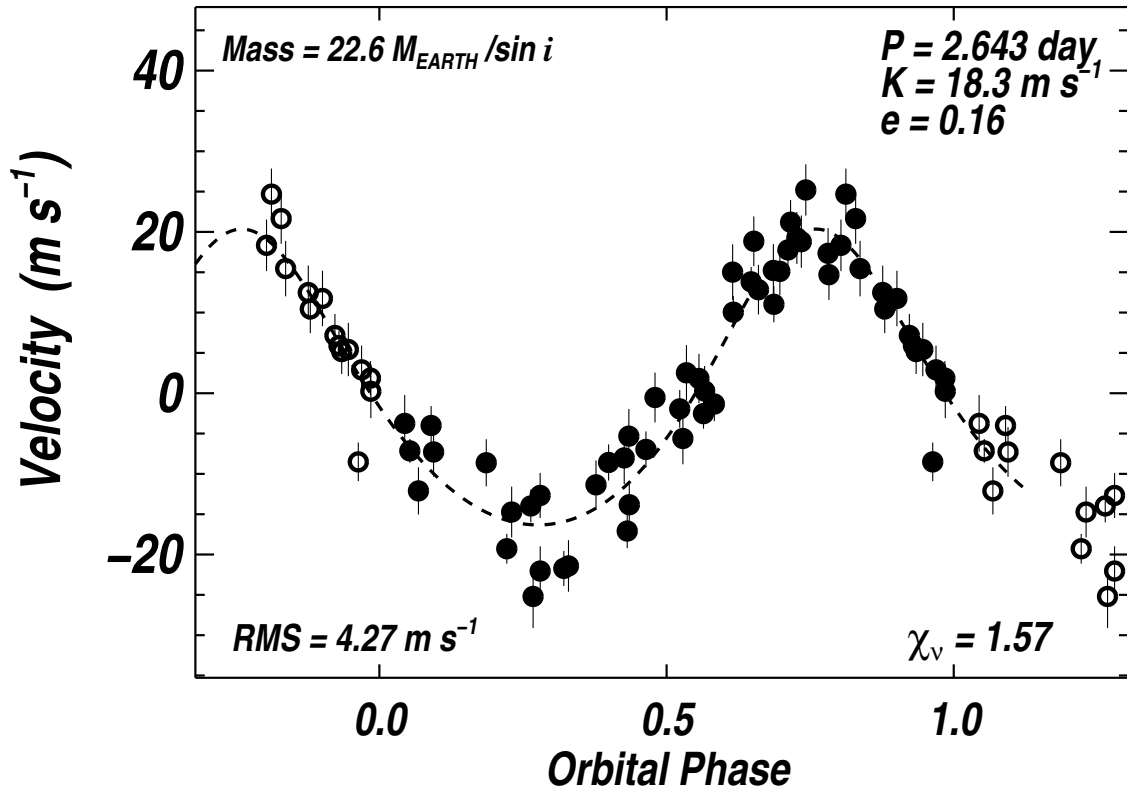


Fig. 6.— Keplerian model plus a linear trend (dashed line) fit to measured velocities (dots) vs. orbital phase for GJ 436. The best-fit orbital parameters are $P = 2.6439$ d, $e = 0.16$, $M \sin i = 0.0713 M_{\text{JUP}} = 22.6 M_{\text{Earth}}$. This model with a linear trend gives the lowest RMS of the residuals, 4.27 m s^{-1} , and the lowest value of $\sqrt{\chi_v^2} = 1.57$.

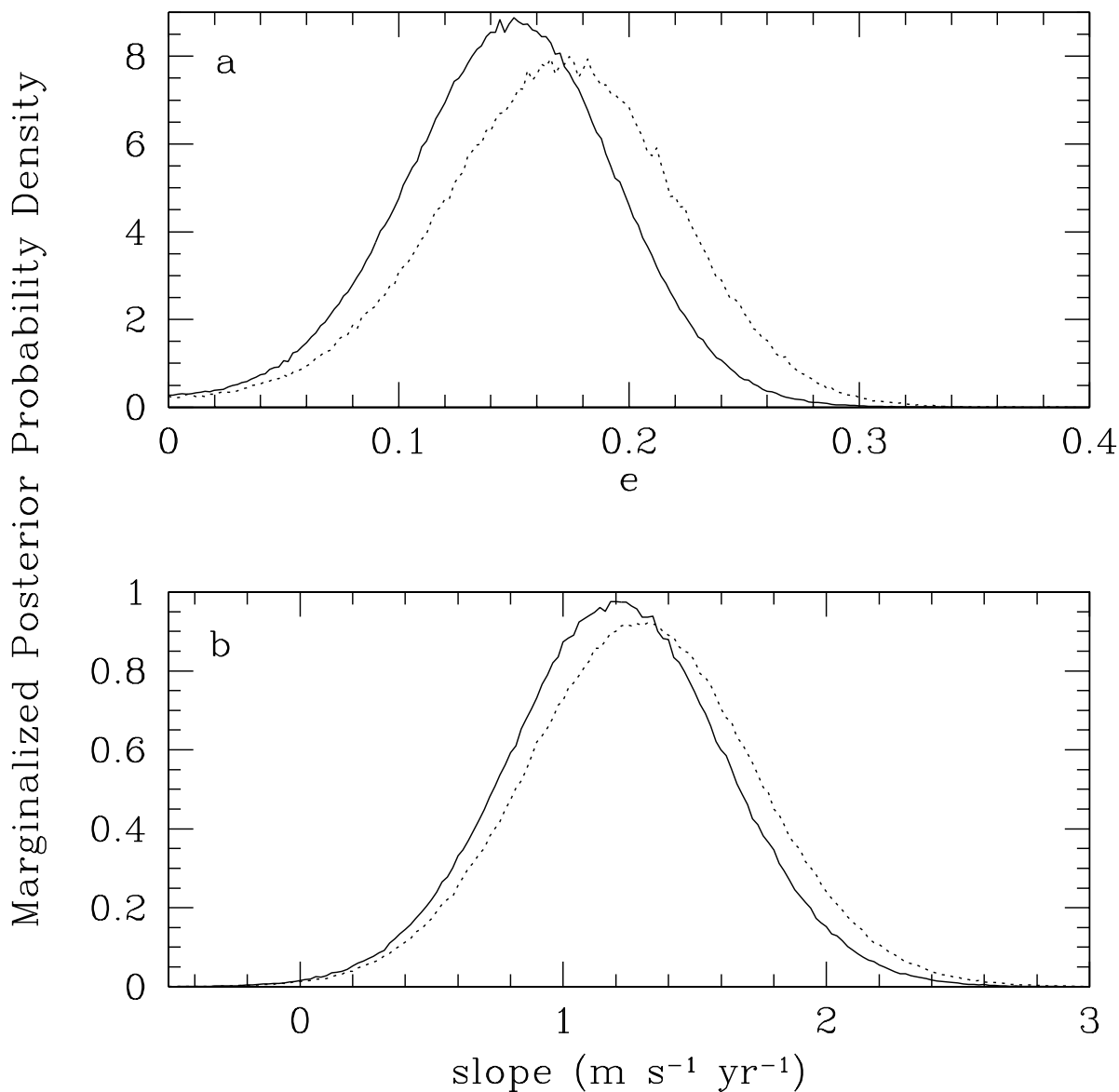


Fig. 7.— The upper panel shows the posterior probability distributions marginalized over all model parameters except the orbital eccentricity for the observations of GJ 436. In the upper panel the solid (dotted) curve assumes a model with (without) a linear slope. The lower panel shows the posterior probability distribution marginalized over all model parameters except the slope. In the lower panel the solid (dotted) curve assumes a model with a slope and a single planet on a Keplerian (circular) orbit.